Saltating motion of a bead in a rapid water stream

Christophe Ancey
Cemagref, Division ETNA, Domaine Universitaire Boîte Postale 76, 38402 Saint-Martin-d'Hères Cedex, France

Françoise Bigillon
2524 Hydrosystem Laboratory, 205 North Mathews Avenue, Urbana, Illinois 61801

Philippe Frey
Cemagref, Division ETNA, Domaine Universitaire Boîte Postale 76, 38402 Saint-Martin-d'Hères Cedex, France

Jack Lanier
Laboratoire Sols Structures Solides, Boîte Postale 53, 38041 Grenoble Cedex 9, France

Rémi Ducret
Cemagref, Division ETNA, Domaine Universitaire Boîte Postale 76, 38402 Saint-Martin-d'Hères Cedex, France
(Received 5 April 2002; published 19 September 2002)

This paper experimentally and numerically investigates the two-dimensional saltating motion of a single large particle in a shallow water stream down a steep rough bed. The experiment is prototypical of sediment transport on sloping beds. Similar to the earlier experimental results on fine particles entrained by a turbulent stream, we found that most features of the particle motion were controlled by a dimensionless shear stress (also called the Shields number) N_{Sh} defined as the ratio of the bottom shear stress exerted by the water flow to the buoyant weight of the particle (scaled by its cross-sectional area to obtain a stress). We did not observe a clear transition from rest to motion, but on the contrary there was a fairly wide range of N_{Sh} (typically 0.001–0.005 for gentle slopes) for which the particle could be set in motion or come to rest. When the particle was set in motion, it systematically began to roll. The rolling regime was marginal in that it occurred for a narrow range of N_{Sh} (typically 0.005–0.01 for gentle slopes). For sufficiently high Shields numbers ($N_{\mathrm{Sh}}>0.3$), the particle was in saltation. The mean particle velocity was found to vary linearly with the square root of the bottom shear stress and here, surprisingly enough, was a decreasing function of the channel slope. We also performed numerical simulations based on Lagrangian equations of motion. A qualitative agreement was found between the experimental data and numerical simulations but, from a quantitative point of view, the relative deviation was sometimes substantial (as high as 50%). An explanation for the partial agreement is the significant modification in the water flow near the particle.

DOI: 10.1103/PhysRevE.66.036306 PACS number(s): 45.50.−j, 47.85.−g, 92.10.Wa

I. INTRODUCTION

Dilute turbulent suspensions are common in both industrial and environmental contexts. Typical examples include heat exchangers, chemical reactors, sprays, dust clouds, particle jets, sediment transport in rivers, estuaries, and oceans, snow or sand drift, dunes, etc. Given how difficult it is to model two-phase turbulent flows, there is no fully satisfactory theoretical framework for computing the bulk flow properties of these suspensions. In attempts to better understand the coupling between the continuous and the dispersed phases together with the role of turbulence, investigation into the motion of a single particle is of great interest since, most of the time, it can provide deeper insight into the main physical mechanisms involved. The motivation for the work reported here was the problem of sediment transport in water free-surface flows (for a modern and physical introduction to this area, see [1]). To that end, we performed extensive experiments on a basic problem: the motion of a single spherical particle in a water flow down an inclined open channel with a rough bottom. The approach followed here is very similar to that developed to understand dry granular flows [2–7].

To date, since this problem is directly connected to engineering problems encountered in sediment transport in rivers and oceans, related papers have described experiments in the laboratory, with conditions very close to those prevailing in nature [8–12]. For instance, natural sediment was used and the size of sediment relative to the typical length of the water flow was low. A number of phenomenological relationships (e.g., the Shields diagram for the threshold of motion initiation [13]) have been derived but the anchorage to the physics of the involved phenomena is weak. Here, to supplement and expand the early observations, we considered the more basic problem of the two-dimensional motion of a spherical particle. In contrast with earlier experiments, we used particles whose size was large compared to the flow depth, so that their motion was not fully controlled by the velocity fluctuations of the turbulent fluid. In doing so, we have introduced the possibility of testing a number of assumptions on the coupling between the continuous and dispersed phases made in theoretical models of the inertial regime (e.g., [14]). Still, in contrast with earlier experiments focusing on horizontal or gently sloping beds, we have examined a fairly wide range of channel slopes to evaluate the effect of gravity on particle

 ©2002 The American Physical Society

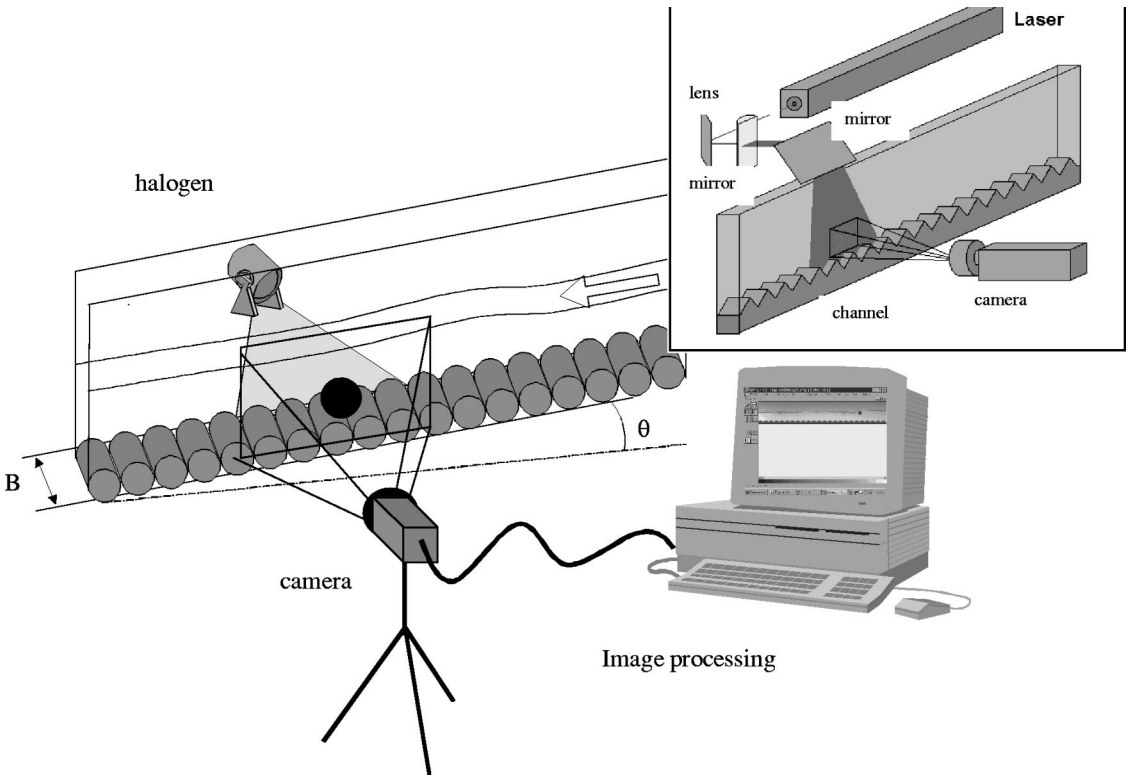

FIG. 1. Definition sketch of the experimental setup.

motion. Moreover, we have tested different types of roughness to evaluate its impact on both turbulence and particle motion.

In the following, Sec. II will be devoted to the presentation of the experimental facility and techniques. In order to facilitate the interpretation of our results, we will present a qualitative overview of our experiments in Sec. III. This includes the introduction of a series of relevant dimensionless numbers and the description of motion regimes. In this article, we focus particular attention on the saltating regime, which was most often observed in our experimental device. The rolling regime is described in a companion paper (see also [15]). The experimental results on the saltating regime will be described in Sec. IV. In Sec. V, we will then compare our data with the predictions of numerical simulations based on a simple Lagrangian equation of motion. Comparing experimental and numerical results directly without tuning any adjustable parameter will be emphasized. In Sec. VI, the same exercise will be made with the threshold of motion initiation.

II. EXPERIMENTAL FACILITIES AND TECHNIQUES

A. Particles

Two classes of spherical particles were used in the experiments: glass beads and steel beads. The particle density ρ_p was, respectively, 2500 and 7750 kg/m^3. Beads were calibrated particles whose nominal diameter $2a$ was either 3 mm or 6 mm.

B. The channel

Experiments were carried out in a tilted, narrow, glass-sided channel, 2 m in length and 20 cm in height. The width W was adjusted precisely to be 1 mm larger than the particle diameter so that the particle motion was approximately two dimensional and stayed in the focal plane of the camera. Uncertainty on the width adjustment all along the channel was less than 2%. The channel inclination ranged from 0° to 20°, but in practice we restricted ourselves to the range 0°–12° because for steep slopes the gravity waves (roll waves) traveled over the free surface of the water stream, which was therefore overly irregular. The channel slope could be adjusted very precisely using a screwjack, with uncertainty less than 0.1%.

Figure 1 is a schema of the experimental facility. The water supply at the channel entrance was controlled by an electromagnetic flow meter provided by Krohne (France). The discharge per unit width q ranged from 0 to 0.019 m^2/s. Uncertainty on the flow rate was less than 0.5%. Typically, this resulted in flow depths h and mean velocities $\overline{u_f}=q/h$ of the order of 0.02 m and 0.5 m/s, respectively; the flow depth was a few particle diameters. Most of the time, for channel slopes in excess of 1°, the water flow regime was supercritical, that is, the Froude number $\mathrm{Fr}=\overline{u_f}/\sqrt{gh}$ (where g denotes the gravity acceleration) exceeded unity. This also means that the water stream was fully controlled by the upstream condition on the water discharge; notably, the disturbances of the free surface caused by the particle could not move far upstream and affect the imposed flow rate.

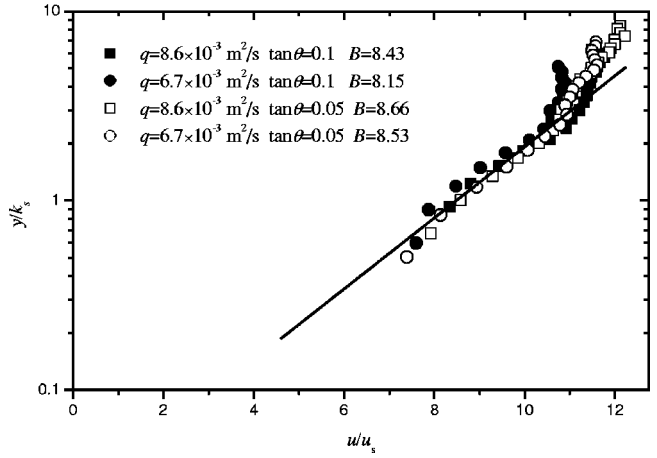

FIG. 2. Velocity profile of the water flow for different slopes and discharges. Measurements performed with a roughness made up of regularly spaced cylinders ($r=1.5$ mm). The solid line represents the logarithmic profile fitted to the data: $u(y)/u_s=\kappa^{-1}\ln(y/y_0)+B$. The fitted value of B is tabulated in the figure key.

The channel base was made up of regularly juxtaposed half cylinders of equal size. We also used random roughness, consisting of half cylinders of various sizes. We selected three sizes of cylinder: their radius r could be either 1.5 mm, 3 mm, or 4 mm. We introduced the roughness parameter as the ratio of the roughness size to the bead radius: $\zeta=r/a$. In the present experimental setup, various disturbing effects arose. First of all, the relative roughness, i.e., the roughness size to the depth of flow ratio, was high, implying that the turbulence was substantially modified by the bottom. Moreover, the channel was narrow: the aspect ratio, defined as the width-to-depth ratio, was less than 5. This implies that the flow could also be substantially modified by the sidewalls. Last, flows were characterized by a fairly low Reynolds number: indeed, the flow Reynolds number, computed as $\mathrm{Re}=4R_H\overline{u_f}/\nu$, ranged from 2000 to 10 000. In the Reynolds number definition, we introduced the hydraulic radius $R_H=Wh/(W+2h)$ and the water kinematic viscosity $\nu=\mu/\rho_f$ (where ρ_f is the water density and μ the dynamic viscosity). In order to verify the existence of a logarithmic velocity profile in our channel, we measured the velocity profile in the direction normal to the bottom. To accomplish this, we used particle image velocity (PIV) techniques: a vertical laser sheet was located at the channel centerline and filmed by a high-speed video camera Pulnix (progressive scan TM-6705AN). The flow was seeded with polyamide particles. We then applied an autocorrelation algorithm to twice exposed images to obtain the velocity profile with uncertainty less than 5%. For the ranges of slopes and discharges tested here, we found that the velocity profiles systematically exhibited a logarithmic zone near the channel bottom. Depending on the discharge and channel slope, this zone extended up to $y/h=0.3$–0.45. This value is to be compared to the usual value of $y/h\approx 0.2$ given in the literature [16]. As shown in Fig. 2, the usual logarithmic law for hydraulically rough bottom fitted the data well:

$$\frac{u(y)}{u_s}=\frac{1}{\kappa}\ln\left(\frac{y}{k_s}\right)+B, \tag{1}$$

where u_s is the friction velocity (also called the shear velocity), $\kappa\approx 0.41$ is the van Kàrmàn constant, and $k_s=4r/3$ is the equivalent size of the roughness. The parameter B was found to lie in the range 7.6–8.7 for $\zeta=1$, that is, close to the typical value of 8.5 given in the literature. Above the logarithmic zone, we observed a blunt transition to a fairly flat profile, as shown in Fig. 2.

In Fig. 2, the friction velocity was deduced experimentally by measuring the slope of the logarithmic part of the velocity profile, which should be equal to u_s/κ. We compared this value to the theoretical value $u_s=\sqrt{R_Hg\sin\theta}$, which only holds for steady uniform flows in very large channels (i.e., when $R_H\approx h$). Since in the present case the sidewalls were very smooth compared to the bottom, their influence on the discharge was limited. Thus, although our channel was narrow, the theoretical value $u_s=\sqrt{R_H\sin\theta}$ provided a correct estimate of the friction velocity measured at the channel centerline. The relative deviation between the two values was less than 20%. We also measured the root mean square velocities in the streamwise and cross-stream directions, u' and v'. We found that for $0.2\leqslant y/h\leqslant 0.8$, the following scalings fitted the data well: $u'=2.3u_se^{-y/h}$ and $v'=1.23u_se^{-y/h}$, in agreement with empirical relationships given in the literature for open-channel flows [16]. It can be concluded that, despite the unusual features of our experimental device, the velocity profile and the main features of the turbulence are not too far from those typically observed in large channels.

In addition to the velocity profile, we determined the discharge equation, that is, the relationship between the flow depth and the flow rate. In practice, the flow depth was measured by using either a rule placed against the sidewall or image processing and measuring the cross-stream distance between the top of the bottom half cylinders and the free surface. In both cases, uncertainty in the flow depth measurement was large due to gravity and capillarity waves along the free surface; typically, uncertainty on the flow depth measurement was within 0.5 mm. We fitted an empirical Darcy-Weisbach friction factor to the data (q,R_H) [17]. We obtained $q=\sqrt{8/f}h\sqrt{gR_H\sin\theta}$, in which $f=0.6\mathrm{Re}^{-0.28}$, a form that is not too far from the Blasius equation used in open-channel and pipe hydraulics ($f=0.223\mathrm{Re}^{-0.25}$). The relative deviation between this fitted equation and data was less than 10%, except for large roughness ($r=3$ mm), where the relative deviation exceeded 40%. From the Darcy-Weisbach equation, we can also deduce the approximate relationship between the mean and friction velocities: $u_s=\sqrt{f/8}\overline{u_f}$. The friction velocity u_s is a weakly nonlinear function of the mean velocity and, at high Reynolds numbers, we have $u_s\approx 0.08\overline{u_f}$.

The motion of the mobile bead was recorded using the Pulnix camera described above. Depending on the selected picture resolution, the frame rate ranged from 60 (resolution of 640×480) to 220 frames per second (resolution of 640×100). Lights were positioned in the back of the channel.

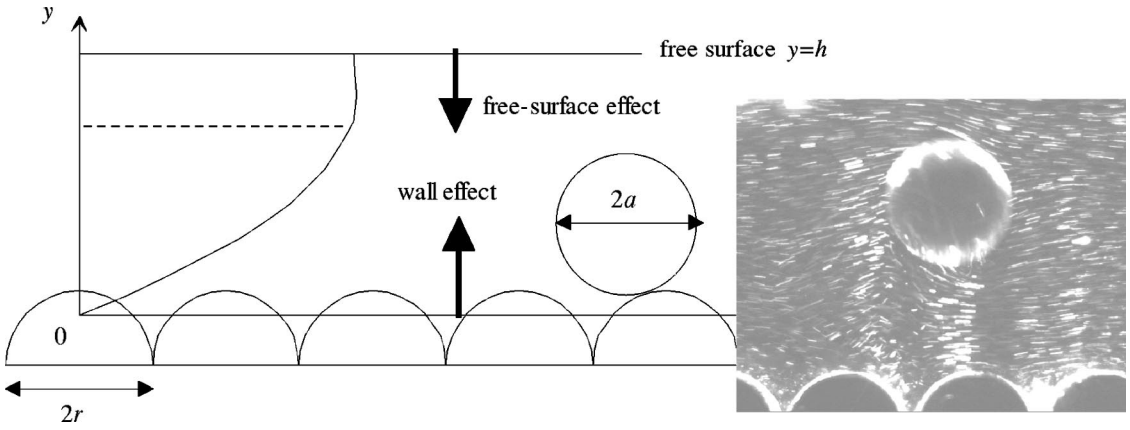

FIG. 3. Schema of the physical system studied here. The panel shows a photograph of a saltating particle (experimental conditions: $q=0.0086$ m^2/s, $\tan\theta=0.1$, $a=3$ mm, glass bead, and $\zeta=1$). The exposure time was 1/500 s. The water flow was seeded with polyamide, whose track gives an idea of the fluid velocity field in the vicinity of the mobile particle.

The panel in Fig. 3 shows a typical photograph of the particle motion and the surrounding fluid. An area 20 cm in length and approximately 5 cm in height was filmed. Images were subsequently analyzed using the WIMA software, provided by the Traitement du Signal et Instrumentation laboratory in Saint-Etienne (France). Resulting uncertainty on the bead position was approximately 0.5 pixels. Typically, 50 to 200 images were required for each run to obtain a sufficiently long series of trajectories. The instantaneous particle velocity **u** was computed as the forward difference between two consecutive positions $\mathbf{x}_i$: $\mathbf{u}_i(t)=(\mathbf{x}_{i+1}-\mathbf{x}_i)/\Delta t$, where Δt was the time between two consecutive frames. Uncertainty on the displacement of the bead between two frames was 1 pixel. To compute the instantaneous bead velocity, the minimum displacement used between two frames was 10 pixels. Thus the uncertainty on the instantaneous bead velocity had a maximum value of 10%.

C. Experimental procedure

A single particle was dropped from above into the water stream 1 m upstream from the measuring window. In order to avoid imparting a momentum to the dropped particle, we gently introduced it into the channel and a honeycomb cell at the channel entrance damped its initial velocity. In addition to instantaneous position and velocity values, we paid specific attention to obtaining averaged values. To that end, experiments were repeated several times to compute time-averaged and ensemble-averaged values. In order to reduce the number of experiments required to obtain meaningful averages, we were interested in determining the minimum number n of runs for which the average value u_n computed over the n runs did not differ appreciably from the value u_{n-1} computed over the $n-1$ previous values. We usually found that the mean velocity converged rapidly toward an asymptotic value. When taking a convergence criterion in the form $|u_n-u_{n-1}|/u_n<0.05$, we found that the asymptotic value was reasonably approximated using $n=3$. Moreover, computation of mean values was meaningful provided the bead reached a steady regime. To examine whether this condition was fulfilled, we measured the mean velocity at three different locations: 30 cm, 80 cm, and 130 cm from the channel entrance. For each location we performed 15 runs with the same flow conditions. Comparison of the three statistical distributions revealed that the mean velocity was fairly constant.

III. QUALITATIVE OVERVIEW OF THE RESULTS

Before detailing the measurements, it may be helpful to provide a qualitative view of the results. To begin with, we will present a series of dimensionless groups that are useful in delineating the flow regimes and describing data. We will then provide an overview of the flow regimes, including a discussion of the physical mechanisms occurring in these regimes as well as an analysis of the common points and differences between the present experiments and similar experiments.

A. The physical system

Figure 3 depicts the motion of the bead in a water stream down a steep channel along with a schema of the two turbulent regimes (see above). Close to the channel bottom, there is a region, most often called the wall region or inner layer, in which the typical scale of velocity is the friction velocity u_s. For a steady uniform flow down an infinite plane, the friction velocity can be directly inferred from the bottom shear stress τ_p: $u_s=\sqrt{\tau_p/\rho_f}$. The region near the free surface is a zone with a highly turbulent dissipation rate. The velocity scale is the maximum mainstream velocity. In the present paper, the mobile particle travels the two regions and sometimes can interact with the free surface. This configuration contrasts with most previous experiments made in closed conduits or open channels, for which the particle was confined within the wall region [8,9,11]. This clearly implies that, in the present context, the moving particle experiences hydrodynamic actions that may differ substantially in nature and strength according to the bead position. This statement must, however, be tempered because the particle size is sufficiently large to modify the turbulence significantly.

B. Dimensionless groups

There is a long tradition and consensus in hydraulics in defining two main dimensionless groups: the Froude number $\mathrm{Fr}=\overline{u_f}/\sqrt{gh}$ and the flow Reynolds number $\mathrm{Re}=4R_H\overline{u_f}/\nu$ [17,18]. It should be noted that in a narrow channel the Froude number is a function of the flow depth h while the Reynolds number depends on the hydraulic radius R_H. In addition to the channel slope, other dimensionless groups can be defined such as the roughness ratio h/r or the roughness Reynolds number $\mathrm{Re}_s=2u_s r/\nu$.

Consensus is probably less marked as regards particle motion, in part because the range of problems and applications is very wide. A survey of the literature devoted to turbulent suspensions, transport of sediment, and granular flows led us to introduce three main dimensionless groups in addition to the channel slope θ and the roughness parameter $\zeta=r/a$: the Reynolds, Stokes, and Shields numbers (also see [19–22]). The particle Reynolds number is $\mathrm{Re}_p=2u_{slip}a/\nu$, where u_{slip} is a velocity scale characterizing the slip velocity of the particle relative to the flow. Different expressions can be used to define the slip velocity, including the terminal velocity of a sphere in a quiescent liquid, the averaged or instantaneous particle-fluid velocity $|u_p-u_f|$, etc. For the present experiments, it seems appropriate to choose the mean particle-fluid velocity $|\overline{u_p}-\overline{u_f}|$. Typically we found that in our experiment the particle Reynolds number lay within the range of 40–4000.

A convenient way of introducing the Stokes number is to define it as the ratio of the particle response time to a representative time of the surrounding flow: $\mathrm{St}=t_p/t_f$. For small particles at low Reynolds numbers, $t_p=2m/(\rho_f u_{slip}\pi a^2 C_D)$ and $t_f=a/u_{slip}$, where $C_D=24/\mathrm{Re}_p$ is the drag coefficient and m is the particle mass, leading to the well-known expression $\mathrm{St}=mu_{slip}/(6\pi\mu a^2)$. For large particles at large Reynolds numbers, we assumed that the above expression of the particle scale time still held true, except that the drag coefficient C_D had to be changed. We further assumed that the characteristic time scale of the fluid was given by the large-eddy passing frequency, that is, $t_f\approx 0.5h/\overline{u_f}$ on average [16]. We then obtained $\mathrm{St}=8m\overline{u_f}/(\rho_f|\overline{u_f}-\overline{u_p}|\pi a^2)$ in which we assumed that $C_D=1/2$ at very high Reynolds numbers and $u_{sl}=|\overline{u_f}-\overline{u_p}|$. The Stokes number is usually interpreted as an indicator of the coupling between the continuous and dispersed phases. Here, with Stokes numbers in the range 20–7000, we deduced that the particle motion was not controlled by the fluid but interacted with it.

These two dimensionless numbers Re and St are used to describe the particle motion and its interactions with the surrounding fluid. The third dimensionless group was introduced to differentiate the cases where the grain is moving from the cases where it is at rest. For small particles relative to the flow depth, a dimensionless group can be formed by comparing the force exerted by the flow (in the streamwise or upward direction) to the buoyant force. The former is approximated as the product of the bottom shear stress and the particle surface exposed to the stream, that is, $F_f=\tau_p\pi a^2=\rho_f u_s^2$. The latter can be expressed as $4(\rho_p-\rho_f)\pi a^3 g/3$. The resulting ratio is called the *Shields number* or *Shields shear stress*: $N_{\mathrm{Sh}}=F_f/F_p\approx\rho_f u_s^2/[2(\rho_p-\rho_f)ag]$. If the particle was a block and the expressions above were exact, it would then be expected that motion would occur when the driving force exerted by the fluid F_f exceeded the tangential force λF_p, where λ is the friction coefficient, whose magnitude is typically around 0.1. In that case, the condition for motion can be expressed in terms of the Shields number as $N_{\mathrm{Sh}}\geqslant 0.1$. In the present context, due to the large size of the particle, it is probably better to replace the friction velocity u_s by the mean flow velocity $\overline{u_f}$ in the expression for F_f. Nonetheless, since it has been shown that the velocities u_s and $\overline{u_f}$ are nearly linearly linked, there is not much difference in choosing one or the other. Thus, in the following, we will keep the usual expression of the Shields number.

Obviously, owing to the large degrees of freedom of the studied system, many other dimensionless groups can be built, but as they do not really contribute to explaining the physics of our problem, we will no longer dwell on this issue.

C. Motion regimes

Transport of particles in water is usually classified into three regimes: rolling/sliding, saltation, and suspension. The same flow pattern was observed in our experiments. The present results and the large amount of data available on particle movement enable us to further clarify some important points in this partitioning.

The threshold of motion initiation marks the limit between incipient motion and rest. In the literature devoted to transport of sediment, this limit is given in the form of a condition on the Shields number [23]. As discussed above, for Shields numbers in excess of a critical value $N_{\mathrm{Sh},c}=f(\mathrm{Re}_p,\theta,\zeta)$, the particle is set in motion. Typically, for a sufficiently large particle lying on a flat horizontal bottom, $N_{\mathrm{Sh},c}$ is very close to 0.05 on average, but the range of possible values is far wider, approximately 0.02–0.2 [13,18]. At first glance, the relative success of this formulation in representing the beginning of motion of small particles is surprising. Indeed, the bottom shear stress is characterized by strong spatiotemporal intermittence due to the development of intense coherent structures (a bursting process consisting of periodic sweeps and upward ejections of fluid from the viscous sublayer) [12,24,25]. The dynamics of incipient motion is then probably controlled by the departures from the mean bottom shear stress τ_p' rather than the mean value $\overline{\tau_p}$. A possible explanation for this success is related to the fact that the bursting period mainly depends on the friction velocity u_s for a flat bottom [26]. Thus, as $\tau_p'\propto u_s^2$ and $\overline{\tau_p}\propto u_s^2$, the beginning of motion is controlled by the Shields number whatever the actual mechanism of entrainment. In the present case, since the bottom is corrugated and the particle size is large, incipient motion mainly results from the loss of equilibrium of the particle [27,28]. In this case, the main hydrodynamic force responsible for motion initiation is

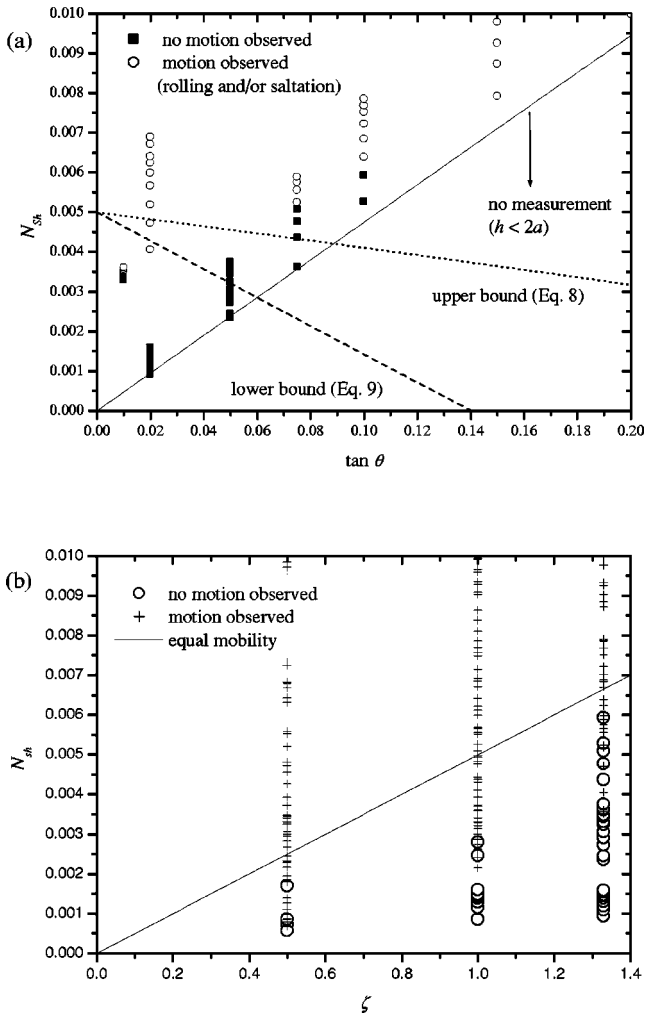

FIG. 4. Threshold of motion initiation. (a) Diagram (N_{Sh},θ) in which experimental conditions for which motion was observed or not are reported. The solid line represents the limiting flow conditions, below which the flow depth is less than the particle diameter. (b) Diagram (N_{Sh},ζ) in which experimental conditions for which motion was observed or not are reported.

the drag force. Due to the dependence of the velocity field on the friction velocity, the drag force is a function of u_s^2 and thus it is still expected that the threshold of motion can be expressed in terms of the Shields number. Figure 4 shows the threshold of motion as a function of the Shields stress and channel slope [subplot (a)] or the bed roughness [subplot (b)]. It was not possible to explore all the space $(N_{\mathrm{Sh}},\tan\theta)$ because we focused our attention on flows for which the flow depth exceeded the particle diameter. Here this required that the Shields number exceed a critical value: $N_{\mathrm{Sh}} \geqslant \sin\theta/[(\rho_p/\rho_f-1)(1+4a/B)]$. The corresponding curve is reported in Fig. 4(a) (solid line). Note that here the critical Shields number is much lower than the value given initially by Shields and subsequent authors (in the range 0.04–0.06 [13,23]). This seems to be an effect of the particle geometry since most authors worked with natural irregular particles (sand and gravel). Experiments performed by Coleman with beads (quoted in [29]) provided values of the critical Shields number in the range 0.002–0.1, consistent with our experiments. A key feature in the diagrams in Fig. 4 is that we did not observe a sharp separation between the flow conditions for which motion occurred and those for which no motion was observed. On the contrary, for a given channel slope and bed roughness, it was possible to define a lower bound of the Shields number, below which we never observed motion, and an upper limit, beyond which motion systematically occurred. In between these two limits, the particle came to rest or was set in motion depending on the flow conditions and the history of the particle motion. For instance, when a particle was primarily at rest, it could be set in motion by increasing the flow rate beyond a critical value q_1, but if we then decreased the flow rate, we had to drop it to a value $q_2<q_1$ for the motion to cease. The two limits for the threshold of motion reflect a kind of hysteretic behavior of the particle (it is not a pure hysteretic behavior since the threshold of motion is also influenced by turbulence fluctuations). This hysteretic behavior is fairly well understood in the context of grain avalanches (e.g., see [7]), where it has been shown that, for the trapping effect of the roughness to be efficient, the kinetic energy of the particle must be low. Figure 4(b) shows that the bed roughness significantly influenced the value of the critical Shields number, in agreement with the earlier investigations of Fenton and Abbott [29], who showed that the critical Shields number depends on the degree of exposure of particles to water flow.

We systematically observed in our experiments that, when the particle was set in motion, it began to roll and/or slide over the bottom roughness. When the water discharge was increased, we observed that the particle could undergo microleaps, notably when it passed from one half cylinder of the roughness to another one. This motivated us to give a more precise definition of the rolling motion. Hereafter, ''rolling motion'' refers to the motion of the bead in sustained contact with the bed; when colliding with a bed particle, the moving bead sometimes underwent a microleap, whose typical length was less than the bead radius a. When the water discharge was increased further, we observed that the microleaps substantially grew in size so that the motion of the bead consisted of a succession of rolling and jumping phases. Finally, when the water flow rate was sufficiently large, the particle no longer rolled but was saltating along the bed. We found few reports in the literature studying the mechanism of the transition from rolling to saltating regimes. In the absence of a water stream, that is, when the surrounding fluid is air, Ancey *et al.* [6] have shown that the centrifugal force could be responsible for the takeoff of the bead. Gordon *et al.* [30] put forward the same idea in the case of a soft plastic ball saltating in a water stream over a rough horizontal bed. The fact that saltation is observed for a wide range of particle shapes and bottom roughnesses (e.g., sand and gravel [11,31]) leads us to think that the centrifugal force is probably not the only mechanism in the takeoff of rolling particles. Another possible mechanism is related to the role played by collisions in the distribution of momentum. When the rolling bead impacts a bed particle, there is a momentum transfer from the downstream direction to the upward direction. The resulting upward impulse is usually balanced by the particle's own weight and the drag force exerted by the fluid.

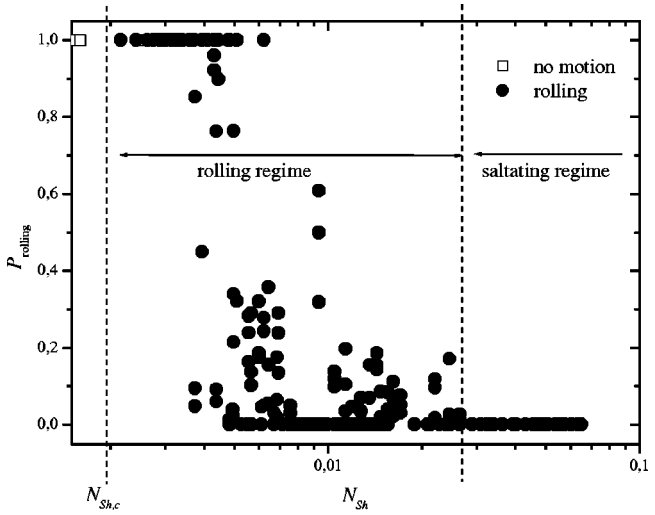

FIG. 5. Empirical probability of observing the particle in the rolling regime as a function of the Shields number. The dashed line represents the upper bound of the critical Shields number above which the particle was systematically in motion.

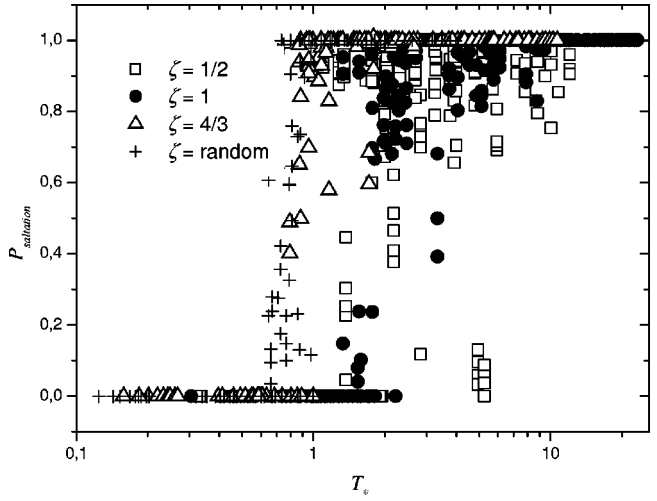

FIG. 6. Empirical probability of observing the particle in the saltating regime as a function of the reduced Shields number for different roughnesses.

In this respect, the microleaps that we observed can be seen as the result of the competition between these forces. In an attempt to quantify these mechanisms crudely, we can estimate that the order of magnitude of the upward collisional force is $F_{up} \propto em\overline{u_p}\chi$, where $\chi \approx \overline{u_p}/(2a)$ is the collision rate and e is the coefficient of restitution. Thus we obtain $F_{up} \propto em\overline{u_p^2}/(2r)$. Using the fact that $\overline{u_p} \propto u_s$ in the rolling regime, we deduce that $F_{up} \propto mu_s^2$. Then, if we try to compare this force to the buoyant force exerted on the particle, once again we find a dimensionless number, whose expression is very close to the Shields number expression. This means that the transition from the rolling regime to the saltating regime should be controlled by the Shields number. Figure 5 shows the proportion of rolling and saltating particles depending on the Shields number. In this figure, the proportion of rolling particles $P_{rolling}$ was computed as the ratio of the time during which the particle rolled to the total duration of the experiment. It is clearly seen in this figure that the rolling regime took place for a narrow range of Shields numbers. For Shields numbers in excess of 0.004, there was first an abrupt decrease in the proportion of rolling particles and then $P_{rolling}$ flattened out and tended toward zero for large Shields numbers. Typically, for Shields numbers in excess of 0.03, one can consider that the particle was in saltation most of the time. We also examined the influence of the channel slope and bed roughness. In order to understand how these two parameters affect the particle motion, it is more interesting to describe the regime occurrence relative to the threshold of motion.

In the following we introduce a reduced Shields number, called the *transport stage*, in the following form: $T_* = N_{\mathrm{Sh}}/N_{\mathrm{Sh},c}$ in which $N_{\mathrm{Sh},c}$ corresponds to the upper bound of the Shields number for motion initiation, so that $T_* > 1$ means that the particle is definitely moving while $T_* < 1$ means that it is at rest or it can be set in motion. Figure 6 shows the proportion of saltating particles as a function of the reduced Shields number for different roughnesses. As for $P_{rolling}$, the proportion of saltating particles $P_{saltation}$ was computed as the ratio of the time during which the particle was in saltation to the total duration of the experiment. The large scatter in the data reflects the relatively large fluctuations in the transition from one regime to another. The data nevertheless define trends, which can be approximated by the naked eye as follows. The larger the roughness parameter ζ, the narrower the range of T_* for which a rolling regime occurs and the more rapid the transition from the rolling to the saltating regime. For instance, for $\zeta = 1/2$, the full rolling regime occurred in the T_* range 0.3–1.5, while for $\zeta = 4/3$ it was not observed at all. When we used a roughness made up of randomly sized half cylinders, we observed that the particle began saltating for $T_* > 0.7$. Similarly, Fig. 7 shows the influence of the channel slope on the transition between the rolling and saltating regimes. For bed slopes in excess of

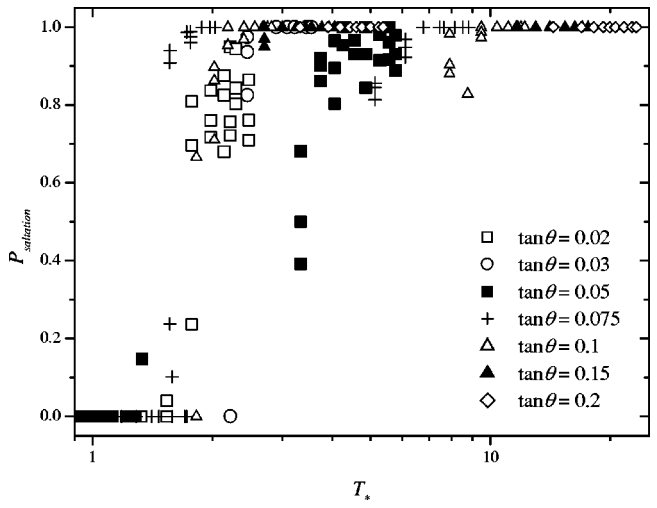

FIG. 7. Empirical probability of observing the particle in the saltating regime as a function of the reduced Shields number for different channel slopes.

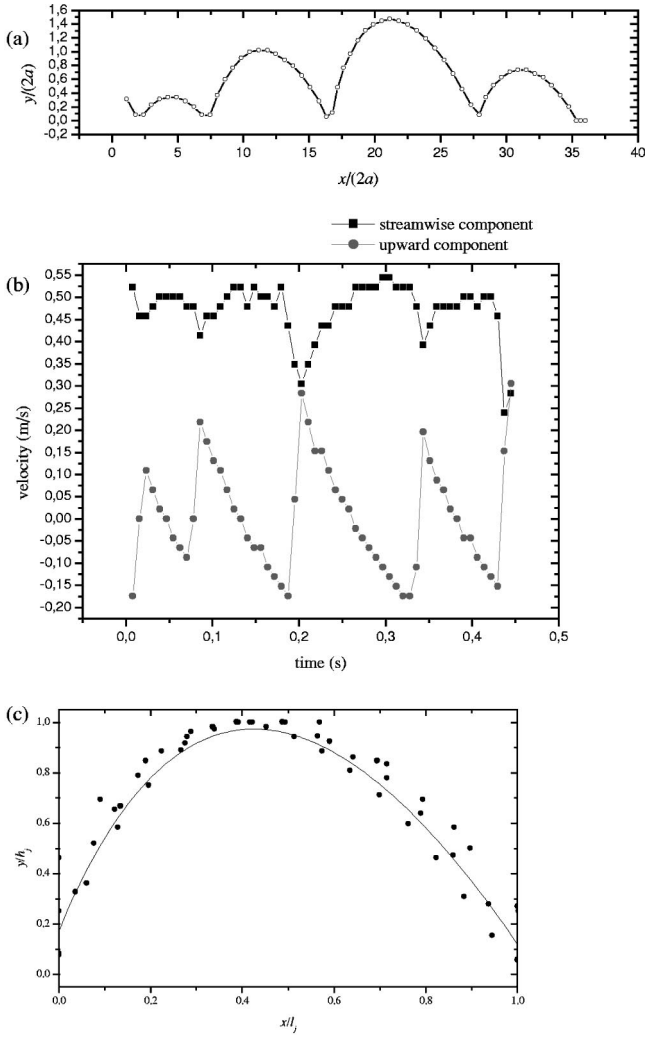

FIG. 8. Sample of trajectories of a glass bead. Experimental conditions: $q=0.0086$ m^2/s, $h=20$ mm, $\tan\theta=0.05$, $a=3$ mm (glass beads), and $\zeta=3/2$. (a) Trajectories reported in a dimensionless form, (b) variation in the downstream and cross-stream components of the particle velocity as a function of the particle position, and (c) scaled trajectories. In panel (c) the solid line represents the parabola of the equation $y=-17.05-12.47+24.12\sqrt{x+0.51}$ (fitted from experimental data).

10%, the rolling regime was not observed; thus, as soon as the particle was entrained by the stream, it started to jump away from the bed. For the slope range 0–10 %, for which a transition from a rolling regime to a saltating regime was observed, no clear trend could be drawn from Fig. 7 as regards the slope effect on the regime transition. For this range of slopes, the transition occurred systematically in the range 1.2–5.

IV. THE SALTATING REGIME: EXPERIMENTAL RESULTS

A. Statistics of saltation trajectories

Typical examples of saltation trajectories are reported in Figs. 8(a) and 8(b), giving the variations in the velocity components as a function of time. The coordinates of the particle

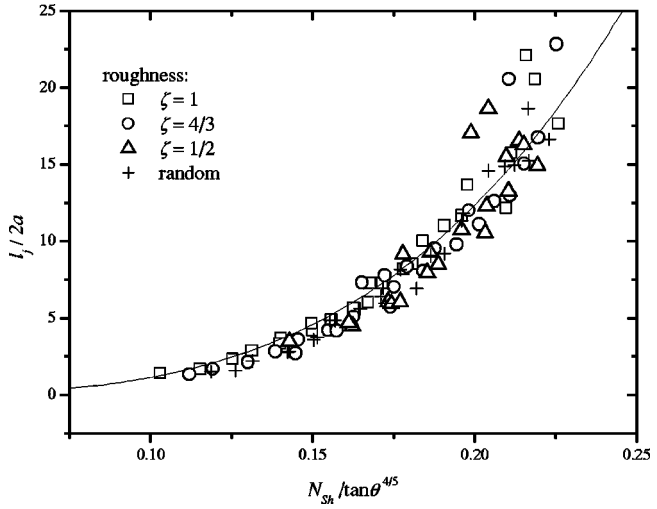

FIG. 9. Variation in the leap length as a function of the scaled Shields stress $\tan\theta^{-4/5}N_{\mathrm{Sh}}$.

mass center were made dimensionless by dividing by the particle diameter. Typically the leaps shown therein are approximately 10 particle diameters in length and 1 particle diameter in height. Surprisingly enough, the trajectory shape is fairly smooth and is apparently not affected by turbulent variations in the surrounding fluid. As seen in Fig. 8(c), the average shape is nearly parabolic and, when scaled by the jump length and height, the experimental trajectories define a single curve. On average the trajectory is nearly parabolic, implying that the streamwise and upward components of the particle velocity vary linearly with time. This is clearly shown in Fig. 8(b) for the upward component: variations in this component with time are sawtooth shaped. Each tooth is composed of a rapidly rising part corresponding to the effect of bed collisions and a slowly decreasing part when the particle comes closer to the free surface and then goes down to the bed. In the case of the upward component, the trend is less marked because of the large fluctuations in the variations of this component. This produces the striking result that the resulting hydrodynamic force acting on the particle is on average constant.

From an analysis of particle trajectories similar to what was presented for Fig. 8(a), we can deduce the geometrical statistical properties of the trajectories according to the flow conditions. The computed geometrical properties include the average (calculated by using the procedure explained in Sec. II C) and the standard deviation of the leap lengths and heights. Examination of the length and height histograms showed that a Gaussian probability distribution fitted the data well, but other bell-shaped probability distributions matched the data as well. Admitting that the main dimensionless number controlling the trajectory features is still the Shields number, we examined variations in the dimensionless length l_j and height h_j of jumps depending on the reduced Shields number, channel slopes, and bed roughness. We found that when we scaled the dimensionless shear stress by $\tan\theta^{4/5}$, almost all the data fell onto a single master curve (see Figs. 9 and 10). This means that the bed roughness had no influence on the jump size. The jump size increased when increasing the ratio $N_{\mathrm{Sh}}/\tan\theta^{4/5}$. The length increased very

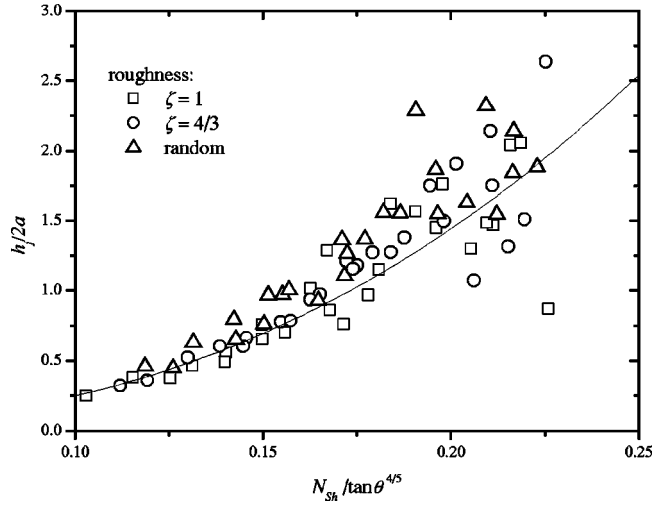

FIG. 10. Variation in the leap height as a function of the scaled Shields stress $\tan\theta^{-4/5}N_{\mathrm{Sh}}$.

quickly and in a nonlinear way with the Shields numbers: $l_j \approx 6260aN_{\mathrm{Sh}}^{3.44}$. In contrast, the master curve for the jump height is much noisier, especially for the highest values of the ratio $N_{\mathrm{Sh}}/\tan\theta^{4/5}$; the general trend can be described by the power-law function $h_j \approx 86aN_{\mathrm{Sh}}^{2.54}$. Probably the best explanation for this data scattering around the master curve is that for large values of $N_{\mathrm{Sh}}/\tan\theta^{4/5}$ the particle came closer to the free surface and thus the jump height was bounded by the flow depth. Despite this crucial difference between our experimental configuration and those used in earlier investigations [32], the overall trends of the variations in the jump size with the Shields number are very similar qualitatively. However, from a quantitative point of view, all the relationships given by the various authors differ. For instance, Lee and Hsu [32] found that $l_j = 392a(N_{\mathrm{Sh}} - 0.026)^{0.788}$ with no effect of the channel slope in the range 0.002–0.023, while van Rijn gave $l_j \approx 200a(N_{\mathrm{Sh}} - 0.05)^{0.9}$ [33].

B. Statistics of collisional interactions with the bed

In order to study the collisional interaction of the particle with the bed, we selected a few images just before and after an impact for different series of leaps. Although the video camera ran at high speed (approximately 200 frames per second), it was nearly impossible to find an image at the time of the impact. Thus, most of the collision features had to be extrapolated from the changes in the trajectories. Another difficulty was that, during a collision, there was a change in both the linear and rotational momentum, but we had no precise measurement of the rotational velocity before and after the collision. It follows that we can infer from the recorded images only the angle of contact ϕ (the angle that the line joining the half cylinder center to the point of contact makes with the normal to the bed), the take-off angle α, and the coefficient(s) of restitution e. The two angles were estimated by evaluating the direction that the normal and streamwise components of the velocity just before and after the impact made with respect to a line perpendicular to the bed. Here the coefficient of restitution e was computed as the ratio of the velocity norms before and after the impact. The statistical properties of the three variables ϕ, α, and e were then evaluated for different channel slopes and flow conditions.

A striking feature of our experiment is the angle of contact ϕ found within a narrow range compared to the range of geometrically possible values $\pm\arcsin[\zeta/(1+\zeta)]$. Moreover, the probability distribution of ϕ was slightly affected by the variations in the flow conditions. Figure 11 shows a typical scaled histogram of the incidence angle for two values of the dimensionless shear stress: the angle ranges from $-10°$ to $35°$ and the most probable values were in the range $15°$–$35°$. Similarly, the take-off angle α was found to be nearly independent of the flow rate. It ranged from $21°$ to $87°$, with a mean value close to $65°$. Its probability distribution was close to an exponential distribution. No correlation was found between the incidence and take-off angles.

It was found that the coefficient of restitution was also slightly dependent on the flow conditions. This can be seen as surprising at first glance but, in fact, this is consistent with the recent studies of Zenit *et al.* [34], Joseph *et al.* [35], and Gondret *et al.* [36] on a colliding sphere against a wall immersed in a Newtonian fluid. These authors have shown that the coefficient of restitution e is an increasing function of the

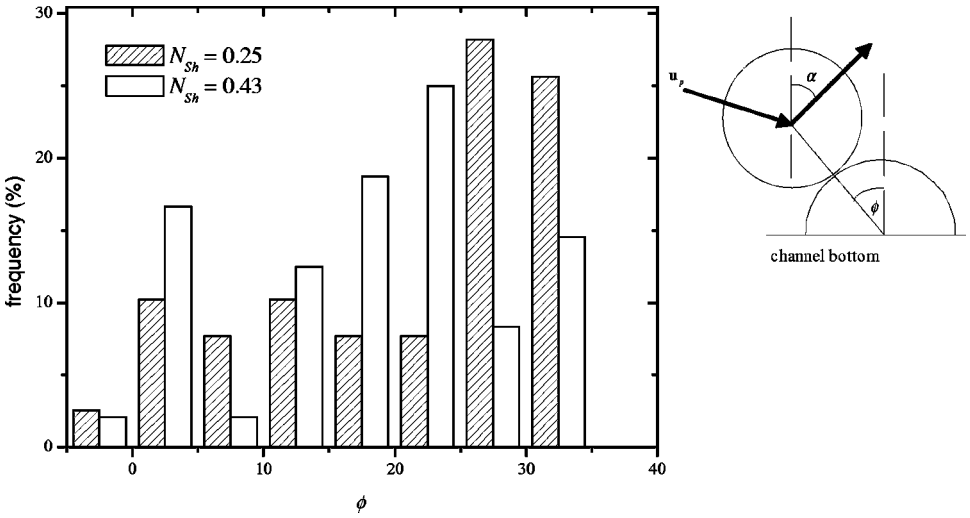

FIG. 11. Histogram of the ϕ values for two values of the Shields stress. Experiments were performed for two values of the Shields number.

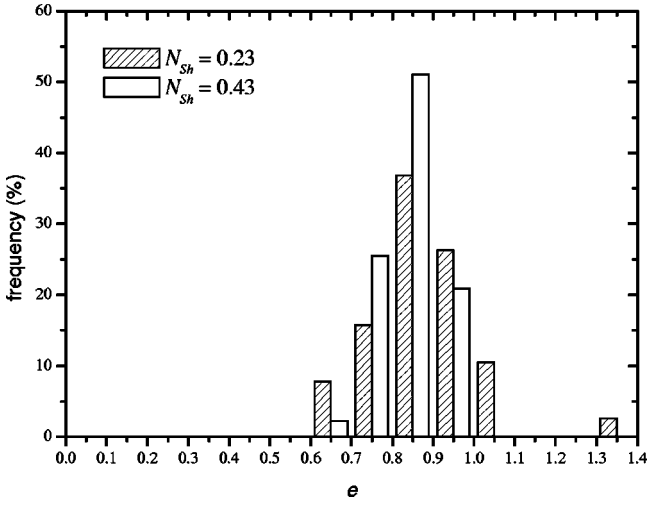

FIG. 12. Histogram of the e values for two values of the Shields stress. Experiments were performed for two values of the Shields number.

Stokes number, with first a rapid increase from 0 to $0.9e_{\max}$, where $e_{\max}$ is the maximum value, when the Stokes number is increased from 1 to 1000, and then a much slower increase for Stokes numbers in excess of 1000. The coefficient of restitution tends asymptotically toward the maximum value $e_{\max}$. Here, for our flow conditions, the Stokes number was high, implying that the coefficient of restitution should be close to the maximum value $e_{\max}$. Figure 12 shows the scaled histogram of the coefficient restitution. The probability distribution was approximately Gaussian. The coefficient of restitution took values over the range 0.6–1.2. When $e>1$, this means that the translational kinetic energy of the particle was increased as a result of the collision, indicating that in some cases there was a transfer of energy from the rotational component of the velocity to its translational component.

C. Streamwise velocity

Figure 13 shows the variations in the mean streamwise velocity as a function of the shear velocity for steel and glass beads. At first glance, when the data are reported in a plot with a linear scale [see Fig. 13(a)], the general trend deduced by the eye is that the mean particle velocity increases as u_s, consistent with earlier experiments on saltating particles over horizontal bottoms [8]. Authors have usually found that the mean particle velocity and the friction velocity are linearly linked: $\overline{u_p}=A(u_s-u_{s,c})$. When fitting this equation to our data, we found that on average for $\zeta=1$ $A\approx 35$ and $u_{s,c}=0.004$ to 0.02 m/s for glass beads and $A=40$ and $u_{s,c}=0.034$ to 0.046 m/s for steel beads. The values found for A and $u_{s,c}$ are much larger than the values given in the literature. For instance, Fernandez-Luque and van Beek [10] found A close to 11.5 for sand, gravel, and magnetite particles while Hu and Hui [37] found A in the range 5.9–11.9. From analyzing a large number of experimental data, van Rijn deduced that the coefficient A depends on the particle diameter since the fluid velocity affecting the particle is much larger than u_s when the particle is large [33]. He found $A=9+0.86\log_{10}\rho_f(\rho_p-\rho_f)gd^3\mu^{-2}$, which here gives $A=14.6$ and $A=15.2$ for steel beads. Here a possible explanation for the enhancement of the coefficients A and $u_{s,c}$ lies in the fact that the channel was narrow. This affected both the water drag on the particle and the water velocity near the particle. To quantify these effects, we performed further experiments. The first experiment involved measuring the settling velocity of the particle in our channel (filled with tap water and in a horizontal position). The drag coefficient [see Eq. (6)] is directly linked to the settling velocity U_{ps} by $C_D=8(\rho_p-\rho_f)ag/(3\rho_f U_{ps})$. We found that for $\mathrm{Re}_p>1000$ the drag coefficient was close to 0.95, that is, a value twice as high as the value usually found for a sphere in an unbounded fluid. In the second series of tests, we measured the variation in the mean water velocity close to the moving particle. For shallow flows, we observed a significant increase in the flow depth near the particle. For the range of slopes and flow rates tested here, we found that the relative increase induced by the particle was $\Delta h=2.1\exp[-1.76h/(2a)]$. However, despite this increase, the flow cross section close to the particle was lower than when far away from the particle. Thus, from the flow rate balance, we deduced that the mean flow velocity was increased by 15% to 30% near the particle.

As shown in Fig. 13(a), the experimental curves $(u_s,\overline{u_p})$ drawn for different values of the channel slope are nearly parallel, indicating that the coefficient A was weakly sensitive to changes in the channel slope, in contrast to the parameter $u_{s,c}$. We found that when the velocity was scaled by $\tan^n\theta$ with $n=1/2$ for glass beads and $n=0.4$ for steel beads, the data fell onto a single curve. In Figs. 13(b) and 13(c), we report the variation in the particle velocity (scaled by $\tan^n\theta$). The half-colored symbols represent experimental runs for which intermittent saltating phases were observed while the blank symbols refer to runs for which the particle was fully in a saltating motion. It clearly appears that when the particle reached a fully saltating regime, its velocity was linearly linked to the friction velocity. For regularly sized roughness and glass beads we found $\overline{u_p}\approx 40(u_s-0.1\tan^{1/2}\theta)$ at sufficiently high friction velocities. For steel beads, we found $\overline{u_p}\approx 40(u_s-0.085\tan^{0.4}\theta)$. It follows that the particle density and the channel roughness have little influence on the particle velocity. For randomly sized roughnesses, the coefficient A is slightly smaller and the data scattering around the mean trend is much more pronounced. In a dimensionless form, the particle velocity can be expressed as $\overline{u_p}/u_s\approx 40(1-S_*^{-1/2})$, where $u_{s,c}\approx 0.1\tan^{1/2}\theta$ and $S_*=u_s^2/u_{s,c}^2$ is a new transport stage (it differs from T_* in that $u_{s,c}$ is not the friction velocity associated with the threshold of motion but the intersection of the linear fitting with the abscissa axis, and thus has no physical meaning). Surprisingly enough, when the channel slope tends toward zero, the structure of the expression above is very similar to the expressions exhibited for gentle slopes [33,38], but the coefficients A do not coincide at all. However, it should be mentioned that in our experimental device and for the range of tested flow rates, the full saltating regime was achieved only for slopes in ex-

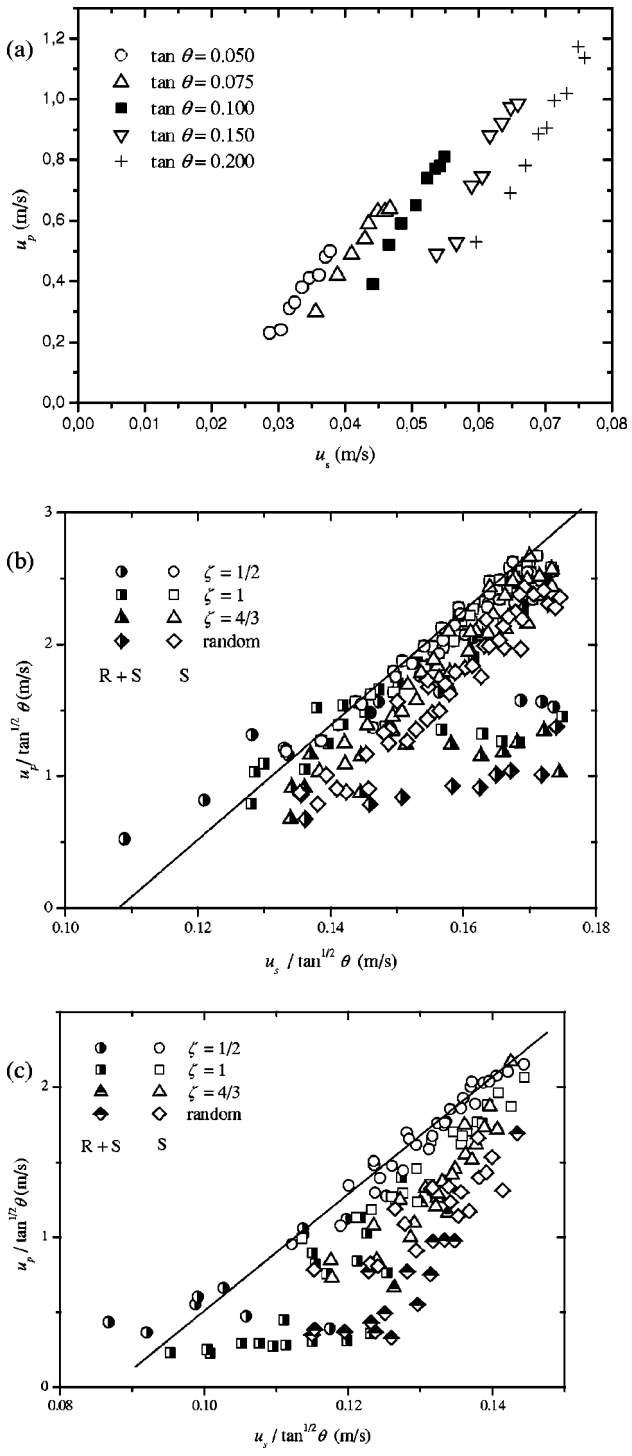

FIG. 13. Variation in the particle velocity. (a) Particle velocity as a function of the friction velocity for different channel slopes in the case of a glass bead in a saltating regime (channel roughness $\zeta=1$). (b) Variation in the particle velocity as a function of the ratio $u_s\tan^{-1/3}\theta$ for different roughnesses in the case of a glass bead; the half-shaded symbols correspond to a particle with intermittent phases of saltation ($R+S$) while the blank symbols represent the data for which the particle was fully in a saltating regime (S). (c) Same as (b) except that the moving bead was a steel bead. The solid line represents the linear relationship $\overline{u_p}/\tan^{1/2}\theta=40(u_s/\tan^{1/2}\theta-0.1)$.

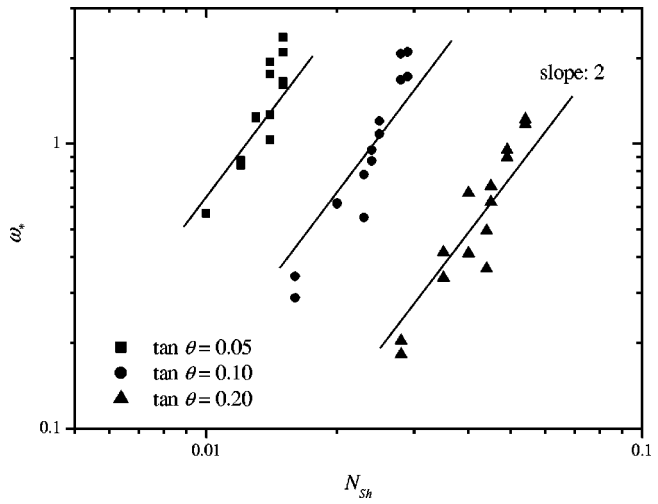

FIG. 14. Variation in the rotational particle velocity as a function of the Shields stress for three different slopes (channel roughness $\zeta=1$).

cess of 0.05, and thus rigorously the expression $\overline{u_p}/u_s \approx 40(1-S_*^{-1/2})$ does not hold for $\tan\theta<0.05$.

In the mixed regime [see half-filled symbols in Figs. 12(b) and 12(c)], there is no clear trend in the variation in the particle velocity with the friction velocity. In contrast with the fully saltating regime, the dependence of the particle velocity on the bed roughness is much more marked. This can be seen, for instance, in Fig. 13(b) by comparing the data related to $\zeta=1/2$ and random roughness: the velocity is twice as high for $\zeta=1/2$ as for random roughness. This dependence has important consequences in terms of sediment transport: for a given roughness, small particles move faster than large particles in this mixed regime, but as soon as they reach the fully saltating regime, they move at the same velocity.

D. Rotational velocity

The particle rotational velocity could be measured since the particle was marked with a strip. When the strip rotation was inscribed in the focal plane of the camera (that is, when it could be seen entirely in a sufficiently long series of images), it was possible to measure the rotational velocity. However, because the spin vector was not systematically normal to the plane of motion, only a limited number of images could be used to measure the rotational velocity.

Figure 14 shows the variation in the dimensionless rotational velocity as a function of the Shields stress. In a steady state, the instantaneous rotational velocity of a small particle in a flow at a finite Reynolds number is directly related to the shear rate: $\omega_p=-\dot{\gamma}/2$ [39]. If that relationship holds here, we expect that the mean dimensionless rotational velocity $\overline{\omega_*}=\omega_p h/\overline{u_f}$ is of the order of unity. In Fig. 14, it is seen that $|\overline{\omega_*}|=O(1)$, but also the data define a trend, which could be approximated very crudely by eye as a linear relationship $\omega_*=\omega h/\overline{u_f}\propto N_{\mathrm{Sh}}^2$ for each channel slope. Moreover, the curves associated with different values of the channel slopes are nearly parallel and far from each other, indicating a large dependence of ω_* on the slope. For instance, on increasing

the channel slope from 0.05 to 0.1, the dimensionless rotational velocity decreases. The scaling $\omega_* \propto N_{\mathrm{Sh}}^2$ contrasts substantially with the only experimental scaling that we found in the literature: indeed, Lee and Hsu [40] found $\omega_* \propto N_{\mathrm{Sh}}^{1/2}$ rather than $\omega_* \propto N_{\mathrm{Sh}}^2$.

V. LAGRANGIAN MODELING OF MOTION

A. Theoretical background

A number of models describing particles saltating in water (or in air) have been proposed over the last two decades [27,41]. Most models are based on two ingredients: (i) a Lagrangian equation of motion describing the particle motion and (ii) a collisional law describing how the impact of the particle with the bed modifies the trajectories. These ingredients are combined and included in the following differential equations describing the variations in the linear and rotational velocities:

$$m\frac{d\mathbf{u}_p}{dt} = m\mathbf{g} + \mathbf{F}(\mathbf{u}_p, \mathbf{u}_f), \tag{2}$$

$$J\frac{d\omega_p}{dt} = \mathbf{G}(\mathbf{u}_p, \mathbf{u}_f) \tag{3}$$

together with the initial conditions $\mathbf{u}_p = \mathbf{u}_{0,i}$ and $\omega_p = \omega_{0,i}$. The subscript i in the initial conditions means that one studies the ith leap of the particle. In Eq. (3), $J = 2ma^2/5$ denotes the inertia moment and ω_f the fluid vorticity. The collisional law χ is introduced through $\mathbf{u}_{0,i}$; the initial velocity $\mathbf{u}_{0,i}$ is also the postcollisional velocity linked to the precollisional velocity $\mathbf{u}_{e,i-1}$ (the terminal velocity of the preceding leap) by $\mathbf{u}_{0,i} = \chi(\mathbf{u}_{e,i-1})$. In Eqs. (2) and (3), the total action of the fluid on the moving particle is represented by the force $\mathbf{F}(\mathbf{u}_p, \mathbf{u}_f)$ and the torque $\mathbf{G}(\mathbf{u}_p, \mathbf{u}_f)$. Usually the interaction between the particle and the fluid is assumed to be sufficiently weak so that the fluid surrounding the particle is not strongly influenced; notably, the fluid velocity field far from the particle is not changed. Generally the motion equation is solved in an iterative way for each leap and then the mean velocities and leap sizes can be inferred. We will now specify the initial conditions and the different terms involved in Eqs. (2) and (3).

The initial condition for the ith leap reflects an exchange of momentum between the saltating particle and the channel roughness. This exchange is usually investigated in the form of a relationship between the pre- and postcollisional relative velocities. In the simplest configuration of a collisional contact (dry collinear collision between two spheres without initial spin), the collisional law takes the form of the well-known Newton law linking the pre- and postcollisional normal components of the relative velocity of mass centers, respectively, c_n and c_n' [42], in a linear way:

$$c_n' = -e_n c_n, \tag{4}$$

where e_n denotes the coefficient of (normal) restitution; $e_n = 1$ when the collision only implies elastic deformations, and $0 < e_n < 1$ otherwise. For more complicated collisional contacts, in an attempt to account for various mechanisms involved (spin effect, hydrodynamic influence, etc.) [34,36,43,44], we can rewrite Eq. (4) in the generalized form $u_{out} = e(\mathrm{St}, u_{in}/(a\omega_p))u_{in}$, where u_{in} and u_{out} denote the norms of the precollisional and postcollisional velocities. Here, since the Stokes number is large and makes allowance for our experimental results, we assume that $e = 0.85$. We further assume that the components of the postcollisional velocities can be expressed as $u_{out,j}(\cos\psi, \sin\psi)$, where $\psi = \pi/2 - \alpha = 35°$ on average; the value of the take-off angle α has been taken as the mean value inferred from our experiments.

Extensive theoretical, numerical, and experimental investigations have been performed to compute the action exerted by a viscous fluid on a spherical particle. This issue is known to be a very difficult one and only partial results are available. The mere formulation of the motion equation of a small single spherical particle in an unbounded viscous fluid in a laminar flow has been widely debated in recent decades. To date, the expression proposed by Maxey and Riley [45] is widely recognized as the most complete and correct equation for that purpose. Accounting for the bounded character of the flow (free surface, solid boundary), nonhomogeneity, weakly or fully developed turbulence, particle spinning, etc. leads to great complexity in the physical formulation, analytical or numerical resolution, and eventually in the applicability to practical problems. Here a major difficulty in considering rapid shallow water flows is that we cumulate all these issues.

Consistent with Maxey and Riley's expression for the Boussinesq-Basset-Ossen equation [45] or Auton *et al.*'s expression for the total force exerted by an inviscid flow [46], the total force can be split into different contributions: $\mathbf{F} = \mathbf{F}_B + \mathbf{F}_{AM} + \mathbf{F}_D + \mathbf{F}_L + \mathbf{F}_P$, in which $\mathbf{F}_B$ denotes the Basset history term (the term arising due to the unsteadiness of the fluid flow close to the particle), $\mathbf{F}_{AM}$ the added-mass effect (the surplus of inertia caused by the relative acceleration, equivalent to the inertia of a virtual mass of fluid attached to the solid particle), $\mathbf{F}_D$ the water drag (Stokes term when $\mathrm{Re}_p = 0$), $\mathbf{F}_L$ the lift force, and $\mathbf{F}_p$ the fluid pressure. If a great deal of work has been successfully expended toward extending Maxey and Riley's formulation of the total fluid force for finite particle Reynolds numbers [47–53], few quantitative results have been provided for large Reynolds numbers (typically for Reynolds numbers exceeding 150) because of the increasingly complex flow pattern, notably in the wake structure. Approximate and empirical relationships must then be used. For $\mathrm{Re}_p > 150$, empirical expressions are available to compute the viscous drag force [54,55]. Here we use

$$\mathbf{F}_D = \rho_f \pi a^2 C_D |u_f - u_p| (\mathbf{u}_f - \mathbf{u}_p)/2, \tag{5}$$

where $C_D = C_D(\mathrm{Re}_p)$. A similar approach could be followed for the torque by writing $\mathbf{G}_D = \rho_f C_T \pi a^5 |\omega_f - \omega_p| (\omega_f - \omega_p)/2$ where the torque coefficient C_T is expressed as a function of the spin Reynolds number $\mathrm{Re}_\omega = a^2|\omega_f - \omega_p|/\nu$. At low Reynolds numbers, this coefficient is given by $C_T = 16/\mathrm{Re}_\omega$ [39]. At finite or large Reynolds numbers, there is

no analytical or empirical estimate of $C_T(\mathrm{Re}_\omega)$. Concerning the lift force, Rubinow and Keller [56] and Saffman [57] demonstrated that a rotating sphere slowly moving in a linear unbounded flow ($\mathrm{Re}_p \ll 1$) is submitted to a lift force orthogonal to its direction of motion: $\mathbf{F}_L = \pi \rho_f \mathbf{u}_p \times \boldsymbol{\omega}_p a^3$. From dimension analysis, Wiberg and Smith [27] deduced an empirical relationship for the lift force in a form close to the drag force expression

$$F_L = \rho_f \pi a^2 C_L (u_T^2 - u_B^2)/2 \tag{6}$$

where C_L is the lift coefficient and u_T and u_B denote the fluid velocity at the top and bottom of the particle, respectively. The lift coefficient is taken to be equal to 1/2 at large Reynolds numbers. Using direct numerical simulations, Kurose and Komori [58] investigated the effects of the fluid shear and particle rotation on the drag and lift forces for $1 \leqslant \mathrm{Re}_p \leqslant 500$. They considered different configurations (particle rotating or not in a sheared or unsheared flow) to evaluate each contribution. They showed that in a linear shear flow the drag coefficient depended on the shear rate and the spin velocity. The dependence was slight (less than 10%) at high Reynolds numbers ($\mathrm{Re}_p > 300$). At high Reynolds numbers, the effects of fluid shear and rotation cannot be treated independently, that is, the drag and lift coefficients of a rotating sphere in a shear flow cannot be directly inferred from the values computed for a stationary sphere in a shear flow or a rotating sphere in a uniform flow. They proposed tabulated relationships relating C_L and C_D to Re_p, ω_p, and $\dot{\gamma}$.

Analytical expressions for the Basset force and added-mass effect are less frequent than those for drag forces and with only a partial agreement with experimental data [59,60]. Concerning the Basset force, Lawrence and Mei [61] demonstrated that the decay rate in the long-established expression of the Basset force depends on which way the particle interacts with its wake. Using numerical simulations (for $\mathrm{Re}_p = 2$ to 150 and $\rho_p/\rho_f = 5$ to 200), Kim *et al.* [49] expressed the history term in the form of a convolution product, in which a kernel expression was fitted to match the low-Reynolds-number asymptotic solutions.

All the expressions above hold for an unbounded fluid. Corrections must be brought in to account for the effect of a solid wall or a free surface [62,63]. Patnaik and co-workers experimentally studied the drag and lift coefficients of a sphere close to or away from a rough or smooth solid boundary at high Reynolds numbers ($3600 \leqslant \mathrm{Re}_p \leqslant 6 \times 10^4$) [64,65]. They found that for a rough boundary the drag coefficient was enhanced by a factor of 1 to 1.2 compared to its value for a unbounded flow. In contrast, they showed that the lift coefficient decreased slightly when the particle Reynolds number was increased. Values ranging from 0.08 to 0.4 were found. The effect of a free surface on the particle motion has received little attention. Sheridan and co-workers reported a complex observed pattern of the particle wake as it approached the free surface [66] ($6000 \leqslant \mathrm{Re}_p \leqslant 9000$). Due to the free surface, vortex shedding differed significantly from that observed in an unbounded fluid. Among other effects, a jetlike flow formed from the top surface of the cylinder and affected the entire wake structure.

For the subsequent calculations, we considered the minimum number of ingredients required to model saltating particles. The lift and drag forces were calculated using Wiberg and Smith's approach [Eqs. (5) and (6)]. The Basset history term was discarded. The added-mass effect was computed by taking the expression given for inviscid fluids (see [67], p. 407). The fluid velocity profile was assumed to be logarithmic over the entire depth; no correction was used to account for the modification in the fluid velocity near the particle or the free surface. Given the difficulty of estimating the actual variation rate in the rotational velocity, its effect was neglected [Eq. (3) discarded]. Thus, in the following, the computations are expected to provide the order of magnitude of the trajectory features. Figure 15 shows typical experimental data and numerical results for leaps sampled at three different slopes. For the initial conditions in the numerical model, we used the values that were experimentally determined. Obviously, the agreement between experiments and simulations is far from complete since we found relative differences as high as 50% for leap lengths and 15% for velocity. However, this very simple model is sufficient to provide the main features of the saltating particle. We also performed extensive sensitivity tests to compare the various expressions proposed for the fluid contributions. One difficulty in these tests was that our experimental conditions were to a more or less large extent far from the conditions for which the theoretical expressions of the Basset or lift forces apply. Leaving this issue aside, we have found that using a sophisticated expression for the lift and drag forces here did not provide better agreement with experimental data. This motivated us to use the simplest expressions for the fluid contributions.

B. Simulation and comparison with experimental data

To simulate a succession of particle hops, we used a stochastic simulation in a way similar to the approach followed by Niño and Garcia [41]. The equation of motion Eq. (2) was solved numerically by imposing specific initial conditions for the particle velocity. As input parameters (ψ, e), we used the values given above: $e = 0.85$, $\psi = 35°$. Numerical simulations were performed for a wide range of flow conditions by varying both the dimensionless shear stress N_{Sh} and the bed slope. For each flow condition, 400 leaps were simulated and the averaged velocity, length, and height were computed over the last 100 leaps (in this way we assume that the averaged values were not influenced by the initial conditions imposed at the beginning of computation). Specific attention was paid to how the slope influenced the particle trajectories. We obtained the following scalings for the dimensionless mean particle velocity, length, and height of leaps: $\overline{u_p^*} = 22.9(1 - S_*^{-0.61}) \approx 14.5(1 - S_*^{-1/2})$ (where $S_* = u_s^2/u_{s,c}^2$ denotes the transport stage, with $u_{s,c} = 0.006$ a critical velocity), $l_j^* = 380 N_{\mathrm{Sh}}^{0.92} - 2.7$, and $h_j^* = 14.9 N_{\mathrm{Sh}}^{0.34} - 2.2$. The order of magnitude of these scalings was comparable with that found for our experimental data; moreover, the general trends (e.g., an approximately linear increase in the particle velocity with the friction velocity) were followed. However, in many respects, the relationships above differed from those found experimentally. First of all, here we found that $\overline{u_p^*}$, l_j^*, and h_j^*

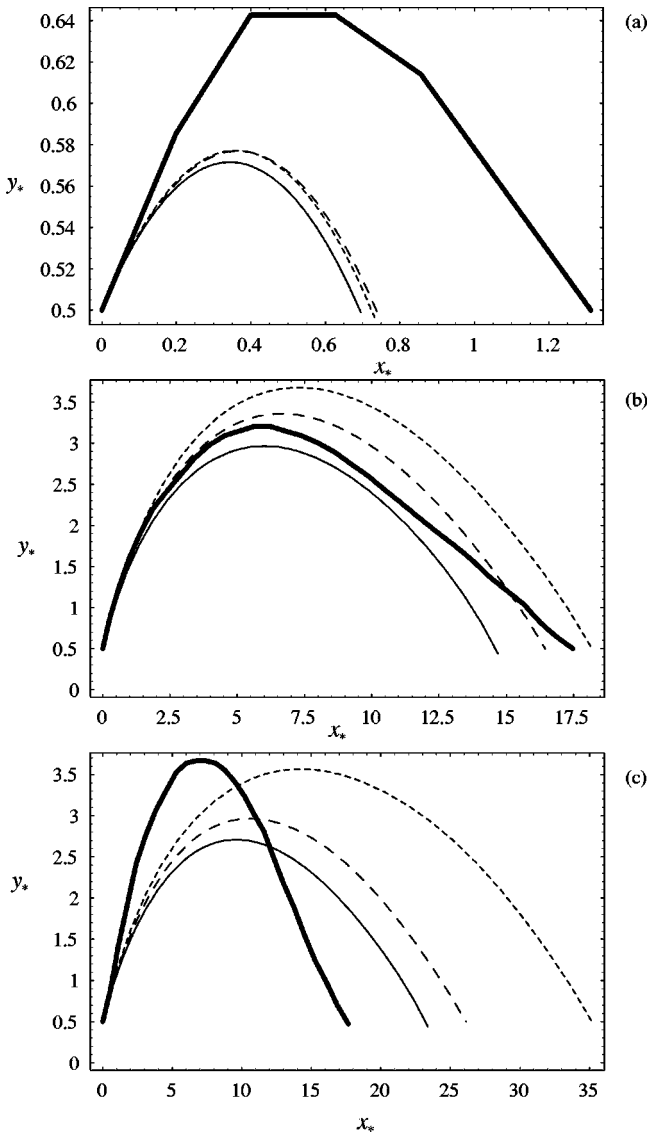

FIG. 15. Typical trajectories at different channel slopes. (a) $\theta = 2\%$, $h = 14$ mm, $q = 0.0028$ m^2/s, $u_0 = 0.17$ m/s (initial velocity), $\psi = 34°$ (Fr$= 0.55$, Re$_f = 2.3\times 10^3$, Re$_p = 340$, $N_{\mathrm{Sh}} = 0.031$). (b) $\theta = 10\%$, $h = 20$ mm, $q = 0.0128$ m^2/s, $u_0 = 0.61$ m/s, $\psi = 54°$ (Fr$= 1.5$, Re$_f = 7.7\times 10^3$, Re$_p = 230$, $N_{\mathrm{Sh}} = 0.227$). (c) $\theta = 20\%$, $h = 12.4$ mm, $q = 0.0128$ m^2/s, $u_0 = 0.82$ m/s, $\psi = 34°$ (Fr$= 3$, Re$_f = 11.3\times 10^3$, Re$_p = 1130$, $N_{\mathrm{Sh}} = 0.277$). Thick lines represent experimentally observed leaps. The thin continuous curves correspond to computations. The continuous curves correspond to the numerical solution obtained using the experimental velocity profile. The dashed curves correspond to the fitted logarithmic velocity profile [Eq. (1)]. The long-dashed curves have been computed using a uniform velocity profile ($\overline{u_f} = q/h$). All the computations were performed using $C_L = 0.2$, C_D provided by Morsi and Alexander's empirical relationships, $\mathbf{F}_B = \mathbf{0}$, and $\omega_p = 0$. The experimental data were made dimensionless by taking $x_* = x/(2a)$ and $y_* = y/(2a)$.

did not depend on the slope whereas in our experiments they did. Moreover, in the numerical simulations, the dependence of the leap size on the Shields number is much less pronounced than in our experiments. More interestingly, the curves that we fitted to our numerical data are fairly close to the experimental scalings provided by van Rijn for gentle slopes and large channels [33]. Using assumptions different from those used in the presented numerical simulations did not change the final results substantially. A possible explanation for the discrepancy between experimental data and numerical simulations is a substantial modification in the fluid velocity profile near the moving particle due to the narrow size of our channel. Further experiments are in progress to examine the reliability of this explanation.

VI. ANALYSIS OF THRESHOLD OF MOTION

In addition to phenomenological relationships fitted to experimental data [13,18], a number of theoretical expressions have been proposed to estimate the critical shear stress for initiating motion of a particle. Most of these models start with an analysis of stability against rotation of a spherical particle lying on a horizontal bed made up of beads of similar size [28,54,68]. Following Wiberg and Smith [68] or Ling [28], if we assume that the particle at rest is submitted to a lift force F_L and drag force F_D in addition to its submerged weight $P = 4\pi(\rho_p - \rho_f) g a^3/3$ and the point of action of the hydrodynamic forces coincides with the center of gravity of the sphere, the balance of moments provides the critical condition for incipient motion of spherical particles: $2\sqrt{2}F_D + F_L = P$. If we consider that the expressions of drag and lift forces are given by Eqs. (5) and (6) and we assume that the mean velocity acting on the particle is $\overline{u_f}$, then we deduce that this condition can be put into the following form (in terms of the Shields number):

$$N_{\mathrm{Sh},c}(\theta = 0) = \frac{f}{12\sqrt{2}C_L + 6C_D}. \tag{7}$$

Extensions have been added to take into account the channel slope and the bed roughness. Chiew and Parker deduced that the critical Shields number at a given slope θ is linked to $N_{\mathrm{Sh},c}(\theta) = N_{\mathrm{Sh},c}(\theta = 0)\cos\theta(1 - \tan\theta/\tan\varphi)$, where φ denotes the particle's angle of repose. From geometrical considerations it is found that $\varphi = \arcsin[\zeta/(1+\zeta)]$ [18] for a particle initially at rest; when the particle comes to rest, this angle can be expressed as $\varphi = \arctan(0.0025e^{7.46\zeta/(1+\zeta)})$. The latter expression was fitted from experiments on a particle rolling down a bumpy line (the surroundings were air) [6]. This allows us to introduce two critical Shields numbers for incipient motion. The first corresponds to the upper limit for which a particle at rest can be observed,

$$N_{\mathrm{Sh},up} = N_{\mathrm{Sh},c}(\theta = 0)\left(\cos\theta - \frac{\sin\theta}{\tan\arcsin[\zeta/(1+\zeta)]}\right). \tag{8}$$

The second critical Shields number corresponds to the lower limit below which no particle comes to rest:

$$N_{\mathrm{Sh},low} = N_{\mathrm{Sh},c}(\theta = 0)\left(\cos\theta - \frac{\sin\theta}{0.0025e^{7.46\zeta/(1+\zeta)}}\right). \tag{9}$$

Usually a multiplying factor is included in these expressions to take into account the influence of roughness. Most of the time, this correcting factor is evaluated from experimental data (e.g., see [69]). An alternative point of view was expressed by Parker, who put forward the notion of equal mobility: on average, for a given bed, the particle begins to move at the same critical shear stress whatever its size [70,71]. In that case, it is expected that $N_{\mathrm{Sh},c}(\zeta)=\zeta N_{\mathrm{Sh},c}(\zeta=1)$. In our experiments (at sufficiently high Reynolds numbers) we have $f\approx 0.05$, $C_D\approx 1$, and $C_L\approx 0.2$; we find $N_{\mathrm{Sh},c}(\theta=0)=0.0053$, a value that seems reasonable when compared to our experimental data [see Fig. 4(a)] when we extrapolated them to vanishing slopes. The upper and lower bounds are found to be decreasing functions of the channel slope. As shown in Fig. 4(a), such a trend is not in agreement with our data: if the variation in the lower bound with slope is hard to assess due to the lack of data at high slopes, the upper limit is found to be an increasing function of the bed slope. A possible explanation of this surprising result is that, in our experimental configuration, the criterion for incipient motion is strongly constrained by the condition $h>2a$. In Fig. 4(b), we report the line $N_{\mathrm{Sh},c}(\zeta)=\zeta N_{\mathrm{Sh},c}(\zeta=1)$ corresponding to the critical Shields number (upper limit) when equal mobility applies. A correct qualitative agreement with our data is found. However, since we tested four values of ζ, the linearity of the critical Shields number with ζ is not proven.

VII. CONCLUDING REMARKS

The objective of this paper was to supplement previous experimental investigations into the motion of heavy solid particles in turbulent fluids in the context of sediment transport. The main differences from previous experimental studies are that (i) the particle was sufficiently large for its motion not to be fully controlled by the fluid velocity fluctuations, (ii) we performed basic experiments in which the two-dimensional motion of a spherical particle was filmed, and (iii) we explored a wide range of channel slopes and bottom roughnesses. Our prototypical experiment was shown to reproduce the main features of sediment transport qualitatively. Interestingly enough, despite the large size of the test particle, the present results do not differ from those obtained with small particles (compared to the flow depth). Notably, it was shown that the Shields number is the key dimensionless number in the entrainment and motion of heavy solid particles in turbulent flows, although the mechanisms involved in incipent motion and suspension depend on the particle size. One possible explanation is that most of these mechanisms are governed by friction velocity, implying in turn that they depend on the Shields number. A surprising result in our experiments is the large dependence of leap height and length on the Shields number compared to previous experimental results and our numerical similations.

Comparing numerical simulations and experimental data has shown that, if a simple Lagrangian model is sufficient to capture the main features of our physical system, agreement is poor from a quantitative point of view since the relative deviation between numerical and experimental data could exceed 50%. Using more sophisticated expressions of the fluid action did not change this conclusion.

ACKNOWLEDGMENTS

This study was supported by the Cemagref and funding was provided by Contrat Plan Etat-Région, Program Avenir of Rhône Alpes Région and by the Program National Risques Naturels of INSU/CNRS, and Action Concertée Incitative ''Risques Naturels'' of CNRS, directed by P. Gondret. We are grateful to the laboratories TSI (Christophe Ducottet, Jacques Jay, and Jean-Paul Schon) and LCPC (François Chevoir) for their help.

[1] N.J. Balmforth and A. Provenzalle, in *Geomorphological Fluid Mechanics*, edited by N.J. Balmforth and A. Provenzalle, Lecture Notes in Physics, Vol. 582 (Springer-Verlag, Berlin, 2001).
[2] G.H. Ristow, F.-X. Riguidel, and D. Bideau, J. Phys. I **4**, 1161 (1994).
[3] S. Dippel, G.G. Batrouni, and D.E. Wolf, Phys. Rev. E **54**, 6845 (1996).
[4] S. Dippel, G.G. Batrouni, and D.E. Wolf, Phys. Rev. E **56**, 3645 (1997).
[5] L. Quartier, B. Andreotti, S. Douady, and A. Daerr, Phys. Rev. E **62**, 8299 (2000).
[6] C. Ancey, P. Evesque, and P. Coussot, J. Phys. I **6**, 725 (1996).
[7] H.M. Jaeger, C. Liu, S.R. Nagel, and T.A. Witten, Europhys. Lett. **7**, 619 (1990).
[8] J.E. Abbott and J.R.D. Francis, Proc. R. Soc. London, Ser. A **284**, 225 (1977).
[9] J.R.D. Francis, Proc. R. Soc. London, Ser. A **332**, 443 (1973).
[10] R. Fernandez Luque and R. van Beek, J. Hydraul. Res. **14**, 127 (1976).
[11] Y. Niño, M. Garcia, and L. Ayala, Water Resour. Res. **30**, 1907 (1994).
[12] Y. Niño and M. Garcia, J. Fluid Mech. **326**, 285 (1998).
[13] J.M. Buffington and D.R. Montgomery, Water Resour. Res. **33**, 1993 (1997).
[14] J.T. Jenkins and H.M. Hanes, J. Fluid Mech. **370**, 29 (1998).
[15] F. Bigillon, Ph.D. thesis, Joseph Fourier University, Grenoble, France, 2001.
[16] I. Nezu and H. Nakagawa, *Turbulence in Open-Channel Flows* (Balkema, Rotterdam, 1993).
[17] V.T. Chow, *Open-Channel Hydraulics* (McGraw-Hill, New York, 1959).
[18] P.-Y. Julien, *Erosion and Sedimentation* (Cambridge University Press, Cambridge, England, 1994).
[19] G.K. Batchelor, in *Theoretical and Applied Mechanics*, edited by P. Germain, J.M. Piau, and D. Caillerie (Elsevier, North-Holland, 1989).
[20] J.R. Fessler and J.K. Eaton, J. Fluid Mech. **394**, 97 (1999).
[21] C. Ancey, P. Coussot, and P. Evesque, J. Rheol. **43**, 1673 (1999).

[22] P. Coussot and C. Ancey, Phys. Rev. E **59**, 4445 (1999).
[23] J. Buffington, J. Hydraul. Eng. **125**, 376 (1999).
[24] B.M. Sumer and R. Deigaard, J. Fluid Mech. **109**, 311 (1981).
[25] J.M. Nelson, R.L. Shreve, S.R. McLean, and T.G. Drake, Water Resour. Res. **31**, 2071 (1995).
[26] T.S. Luchik and W.G. Tiederman, J. Fluid Mech. **174**, 529 (1987).
[27] P.L. Wiberg and J.D. Smith, J. Geophys. Res. (C4) **90**, 7341 (1985).
[28] C.-H. Ling, J. Hydraul. Eng. **121**, 472 (1995).
[29] J.D. Fenton and J.E. Abbott, Proc. R. Soc. London, Ser. A **352**, 523 (1977).
[30] R. Gordon, J.B. Carmichael, and F.J. Isackson, Water Resour. Res. **8**, 444 (1972).
[31] Y. Niño and M. Garcia, J. Hydraul. Eng. **124**, 1014 (1998).
[32] H.-Y. Lee and I.-S. Hsu, J. Hydraul. Eng. **120**, 831 (1994).
[33] L. van Rijn, J. Hydraul. Eng. **110**, 1431 (1985).
[34] R. Zenit and M.L. Hunt, J. Fluids Eng. **121**, 179 (1999).
[35] G.G. Joseph, R. Zenit, M.L. Hunt, and A.M. Rosenwinkel, J. Fluid Mech. **433**, 329 (2001).
[36] P. Gondret, M. Lance, and L. Petit, Phys. Fluids **34**, 643 (2002).
[37] C. Hu and Y. Hui, J. Hydraul. Eng. **122**, 245 (1996).
[38] J.S. Bridge and D.F. Dominic, Water Resour. Res. **20**, 476 (1984).
[39] S. Kim and S.J. Karrila, *Microhydrodynamics: Principles and Selected Applications* (Butterworth-Heinemann, Stoneham, MA, 1991).
[40] H.-Y. Lee and I.-S. Hsu, J. Hydraul. Eng. **122**, 587 (1996).
[41] Y. Niño and M. Garcia, Water Resour. Res. **30**, 1915 (1994).
[42] K.L. Johnson, *Contact Mechanics* (Cambridge University Press, Cambridge, England, 1985).
[43] R.H. Davis, J.-M. Serayssol, and E.J. Hinch, J. Fluid Mech. **209**, 479 (1986).
[44] S. Foerster, M. Louge, H. Chang, and K. Allia, Phys. Fluids **6**, 1108 (1994).
[45] M.R. Maxey and J.J. Riley, Phys. Fluids **26**, 883 (1983).
[46] T.R. Auton, J.C.R. Hunt, and M. Prud'homme, J. Fluid Mech. **197**, 241 (1988).
[47] C.F.M. Coimbra and R.H. Rangel, J. Fluid Mech. **370**, 53 (1998).
[48] V. Armenio and V. Fiorotto, Phys. Fluids **13**, 2437 (2001).
[49] I. Kim, S. Elghobashi, and W.A. Sirignano, J. Fluid Mech. **367**, 221 (1998).
[50] R. Natarajan and A. Acrivos, J. Fluid Mech. **254**, 323 (1993).
[51] J.S. Wu and G.M. Faeth, AIAA J. **31**, 1448 (1993).
[52] A.G. Tomboulides and S.A. Orszag, J. Fluid Mech. **416**, 45 (2000).
[53] T.A. Johnson and V.C. Patel, J. Fluid Mech. **378**, 19 (1999).
[54] W.H. Graf, *Hydraulics of Sediment Transport* (Water Resources Publications, Littleton, CO, 1984).
[55] S.A. Morsi and A.J. Alexander, J. Fluid Mech. **55**, 193 (1972).
[56] S.I. Rubinow and J.B. Keller, J. Fluid Mech. **11**, 447 (1961).
[57] P.G. Saffman, J. Fluid Mech. **22**, 385 (1965).
[58] R. Kurose and S. Kumori, J. Fluid Mech. **384**, 183 (1999).
[59] N. Mordant and J.-F. Pinton, Eur. Phys. J. B **18**, 343 (2000).
[60] E.J. Chang and M.R. Maxey, J. Fluid Mech. **303**, 133 (1995).
[61] C.J. Lawrence and R. Mei, J. Fluid Mech. **283**, 307 (1995).
[62] M.A. Riszk and S.E. Eighobashi, Phys. Fluids **28**, 806 (1985).
[63] D. Hall, J. Fluid Mech. **187**, 451 (1988).
[64] P.C. Patnaik, N. Vittal, and P.K. Pande, J. Hydraul. Res. **30**, 389 (1992).
[65] P.C. Patnaik, N. Vittal, and P.K. Pande, J. Hydraul. Res. **30**, 471 (1992).
[66] J. Sheridan, J.C. Lin, and D. Rockwell, J. Fluid Mech. **330**, 1 (1997).
[67] G.K. Batchelor, *An Introduction to Fluid Dynamics* (Cambridge University Press, Cambridge, England, 1967).
[68] P.L. Wiberg and J.D. Smith, Water Resour. Res. **23**, 1471 (1987).
[69] P.L. Patel and K.G. Ranja Raju, J. Hydraul. Res. **37**, 389 (1999).
[70] G. Parker, P.C. Klingeman, and D.G. McLean, J. Hydraul. Eng. **108**, 544 (1982).
[71] G. Parker and C.M. Toro-Escobar (unpublished).